© 2020. Published by The Company of Biologists Ltd | Journal of Cell Science (2020) 133, jcs241455. doi:10.1242/jcs.241455

RESEARCH ARTICLE

The ubiquitin hydrolase Doa4 directly binds Snf7 to inhibit recruitment of ESCRT-III remodeling factors in *S. cerevisiae*

Dalton Buysse[1], Anna-Katharina Pfitzner[2], Matt West[1], Aurélien Roux[2,3] and Greg Odorizzi[1,*]

ABSTRACT

The ESCRT-III protein complex executes reverse-topology membrane scission. The scission mechanism is unclear but is linked to remodeling of ESCRT-III complexes at the membrane surface. At endosomes, ESCRT-III mediates the budding of intralumenal vesicles (ILVs). In *Saccharomyces cerevisiae*, ESCRT-III activity at endosomes is regulated through an unknown mechanism by Doa4, an ubiquitin hydrolase that deubiquitylates transmembrane proteins sorted into ILVs. We report that the non-catalytic N-terminus of Doa4 binds Snf7, the predominant ESCRT-III subunit. Through this interaction, Doa4 overexpression alters Snf7 assembly status and inhibits ILV membrane scission. *In vitro*, the Doa4 N-terminus inhibits association of Snf7 with Vps2, which functions with Vps24 to arrest Snf7 polymerization and remodel Snf7 polymer structure. *In vivo*, Doa4 overexpression inhibits Snf7 interaction with Vps2 and also with the ATPase Vps4, which is recruited by Vps2 and Vps24 to remodel ESCRT-III complexes by catalyzing subunit turnover. Our data suggest a mechanism by which the deubiquitylation machinery regulates ILV biogenesis by interfering with ESCRT-III remodeling.

KEY WORDS: ESCRT-III, Ubiquitin, Endosome, Membrane, Scission

INTRODUCTION

ESCRT-III is a cellular machine that functions within membrane necks to perform reverse-topology membrane scission, a process wherein membrane-enclosed compartments bud away from the cytosol (reviewed in Schöneberg et al., 2016). Originally discovered in *Saccharomyces cerevisiae*, ESCRT-III is conserved throughout eukaryotes and some archaebacteria. Membrane scission by ESCRT-III functions in diverse cellular processes, including cytokinesis, viral budding and nuclear envelope repair, although ESCRT-III was first characterized based on its role in the budding of intralumenal vesicles (ILVs) at endosomes (Babst et al., 2002). Ubiquitylated transmembrane proteins targeted for lysosomal degradation are sorted into ILVs by ESCRT complexes 0, I and II, all of which contain ubiquitin-binding domains (Alam et al., 2004; Bilodeau, et al., 2002; Katzmann et al., 2001). Transmembrane protein cargos are thought to be trapped at the site of ILV budding by ESCRT-III (Teis et al., 2010), the subunits of which polymerize in a spiral pattern at the membrane surface (Hanson et al., 2008). The assembly of ESCRT-III polymers also constricts and severs the neck of invaginations to complete the ILV budding process (Adell et al., 2014; Schöneberg et al., 2018). Prior to membrane scission, ILV cargos are deubiquitylated by ubiquitin hydrolases, which is necessary to replenish the cellular supply of unconjugated ubiquitin (Swaminathan et al., 1999).

The four core subunits that comprise ESCRT-III in yeast are Vps20, Snf7, Vps2 and Vps24. These subunits are recruited as monomers from the cytosol to the membrane, where they assemble into polymers. The canonical pathway of ESCRT-III complex assembly entails Vps20 nucleation of Snf7 homopolymerization (Saksena et al., 2009; Teis et al., 2008), although other nucleation mechanisms exist (Tang et al., 2016). Snf7 homopolymerization is terminated by its association with Vps2 and Vps24 (referred to herein as Vps2:24) (Teis et al., 2008). *In vitro*, Vps2:24 remodels the Snf7 polymer from a flat spiral into a helical conformation, which might facilitate membrane constriction and/or scission (Chiaruttini et al., 2015; Henne et al., 2012). Vps2:24 also recruits and activates the AAA-type ATPase, Vps4 (Babst et al., 2002; Obita et al., 2007; Stuchell-Brereton et al., 2007). *In vitro*, Vps4 catalyzes Vps2:24 dissociation from polymeric Snf7, which remodels ESCRT-III by promoting further Snf7 polymerization through rapid turnover between membrane-bound and soluble Snf7 subunits (Mierzwa et al., 2017). *In vivo*, Vps4 ATPase activity is essential for membrane scission by ESCRT-III (Adell et al., 2014; Cashikar et al., 2014; Sachse et al., 2004; Wemmer et al., 2011). Collectively, these data suggest that the membrane scission mechanism is driven by remodeling of ESCRT-III complexes achieved by the cooperative actions of Vps2:24 and Vps4.

Vps4 has a microtubule interacting and trafficking (MIT) domain that binds one of two MIT-interacting motif (MIM) sequences located in each ESCRT-III subunit (Kieffer et al., 2008; Obita et al., 2007; Stuchell-Brereton et al., 2007). In some subunits, MIM sites not bound by Vps4 serve as binding sites for other MIT-containing proteins, including ubiquitin hydrolases that deubiquitylate ILV cargos. MIT–MIM interactions mediate recruitment of two distinct ubiquitin hydrolases in humans, USP8 (also known as UBPY) and AMSH (officially known as STAMBP) (McCulloughe et al., 2004; Row et al., 2006). The USP8 ortholog in yeast is Doa4, which has a predicted MIT domain through which it binds the MIM1 site in Vps20 (Richter et al., 2013). Its interaction with Vps20 does not mediate Doa4 recruitment but, instead, inhibits ILV cargo deubiquitylation, suggesting that Vps20 represses ubiquitin removal at the onset of ESCRT-III assembly (Johnson et al., 2017).

In addition to its role in cargo deubiquitylation, Doa4 functions through a poorly understood mechanism to regulate ESCRT-III membrane scission activity (Johnson et al., 2017; Richter et al., 2013). When overexpressed in yeast, Doa4 inhibits ILV membrane scission and increases the size and abundance of Snf7 polymers (Johnson et al., 2017). These observations suggest that Doa4 inhibits ESCRT-III function by affecting remodeling of the complex. This role of Doa4 does not depend on its ubiquitin hydrolase activity or its interaction with Vps20 (Johnson et al.,

[1]Department of Molecular, Cellular, and Developmental Biology, University of Colorado, Boulder, CO 80309, USA. [2]Department of Biochemistry, University of Geneva, Geneva CH-1211, Switzerland. [3]Swiss National Centre for Competence in Research Program Chemical Biology, Geneva CH-1211, Switzerland.

*Author for correspondence (odorizzi@colorado.edu)

A.-K.P., 0000-0001-9952-5525; A.R., 0000-0002-6088-0711; G.O., 0000-0002-1143-1098

Received 7 November 2019; Accepted 2 March 2020

Journal of Cell Science (2020) 133, jcs241455. doi:10.1242/jcs.241455

2017), which hints at regulation of ESCRT-III by other means. Here, we show that Doa4 binds the Snf7 subunit of ESCRT-III and that, through this interaction, Doa4 overexpression in yeast causes accumulation of Snf7 polymer assemblies and inhibits ILV membrane scission. We further show that the interaction between Doa4 and Snf7 prevents association of the Vps2:24 subcomplex that works with Vps4 to remodel ESCRT-III complexes.

RESULTS

Snf7 MIM1 binds the N-terminus of Doa4

We explored the possibility that ESCRT-III is regulated through direct contact with Doa4, based on observations that Snf7 interacts with Doa4 in yeast two-hybrid assays and in protein microarrays (Bowers et al., 2004; Wolters and Amerik, 2015). We initially tested whether Snf7 binds *in vitro* to the N-terminal MIT-like domain of Doa4 – amino acids 1-80 (Fig. 1A) that was identified based on its predicted structural similarity to MIT domains from other proteins (Richter et al., 2013). However, a recombinant GST fusion protein containing the Doa4 MIT-like domain (GST-Doa4$^{1\text{-}80}$) did not bind *in vitro* to Snf7; neither did it bind Vps2 or Vps24 (Fig. 1B). Only the Vps20 subunit of ESCRT-III bound GST-Doa4$^{1\text{-}80}$ (Fig. 1B), as previously described (Richter et al., 2013).

Located near the Doa4 MIT is a rhodanese homology domain (RHD; amino acids 205-328), which is a conserved domain superfamily found in diverse eukaryotic and bacterial proteins (Fig. 1A). Snf7 bound a GST-tagged fragment of Doa4 that included both the MIT and RHD (GST-Doa4$^{1\text{-}348}$) but not a smaller region of Doa4 that encompassed the RHD but lacked the MIT (GST-Doa4$^{107\text{-}348}$; Fig. 1B). In subsequent experiments of this study, we focused on Snf7 binding to the Doa4 region comprising amino acids 1-348.

Neither Vps2 nor Vps24 bound GST-Doa4$^{1\text{-}348}$, and they did not bind GST-Doa4$^{107\text{-}348}$ either (Fig. 1B). Vps20 also failed to bind GST-Doa4$^{1\text{-}348}$, even though it bound the smaller Doa4 fragment within GST-Doa4$^{1\text{-}80}$ (Fig. 1B). We have previously observed a similar loss of Vps20-binding when the Doa4 MIT was lengthened beyond Ala^{80} (Richter et al., 2013), indicating the binding activity of this domain is sensitive to amino acids flanking it.

We explored the molecular basis of Snf7 binding to Doa4$^{1\text{-}348}$ by testing the extent to which this interaction requires one of the two MIM sequences of Snf7 (Fig. 1A). MIM2 binds the MIT domain of the Vps4 ATPase (Adell et al., 2014; Kieffer et al., 2008). A point mutation of MIM2 (ΔMIM2), however, did not affect Snf7 binding to Doa4$^{1\text{-}348}$ (Fig. 1C). MIM1 of Snf7 binds Bro1 (McCullough et al., 2008; Wemmer et al., 2011), a cofactor that stimulates the Doa4 ubiquitin hydrolase activity (Richter et al., 2013). Binding of Snf7 to Doa4$^{1\text{-}348}$ was disabled by a point mutation of MIM1 (ΔMIM1) or upon deletion of the MIM1-containing helix α6 (Δhelix6) (Fig. 1C). Direct binding of the Doa4 N-terminus to Snf7, therefore, depends on the MIM1 sequence of Snf7, which also binds Bro1.

We next assessed the extent to which Doa4 binding to Snf7 could be detected at yeast endosomes by using bimolecular fluorescence complementation (BiFC). The coding sequences of the N- or C-terminal fragments of Venus fluorescent protein (VN or VC, respectively) were chromosomally integrated in frame with *DOA4* and *SNF7* genes, yielding the C-terminal fusion proteins (Doa4-VN and Snf7-VC, respectively), each of which expressed under control of its endogenous genomic promoter. Binding between Doa4 and Snf7 would bring VN and VC into close proximity, allowing the Venus reporter to fold into its native structure and emit fluorescence (Kerppola, 2006). C-terminal VN- or VC-tagging of ESCRT-III subunits renders them non-functional with respect to ILV cargo sorting (Fig. S1) but does not disrupt their subcellular localization on endosomal and vacuolar membranes, making them useful for testing direct protein interactions *in vivo*. Wild-type yeast coexpressing Doa4-VN and Snf7-VC exhibited BiFC fluorescence at discrete puncta located adjacent to vacuoles stained with FM 4-64 (Fig. 1D). This BiFC signal was strongly reduced when Doa4 or Doa4$^{1\text{-}348}$ were overexpressed from a high-copy (2 μ) plasmid, which enabled untagged Doa4 to outcompete Doa4-VN in its interaction with Snf7-VC (Fig. 1D,E). Likewise, BiFC fluorescence was reduced by a point mutation of Snf7 MIM1 (Snf7$^{\Delta MIM1}$-VC; Fig. 1D,E), consistent with requirement of the MIM1 sequence in Snf7 for binding between Doa4 and Snf7 (Fig. 1C). Coexpression of Doa4$^{1\text{-}348}$-VN with Snf7-VC also yielded discrete fluorescent puncta (Fig. 1D), which were significantly brighter than when full-length Doa4-VN was coexpressed with Snf7-VC (Fig. 1E), suggesting that the C-terminal region of Doa4 might negatively regulate its interaction with Snf7.

Doa4 localization to endosomal puncta is strongly reduced in the absence of its catalytic cofactor Bro1 (Luhtala and Odorizzi, 2004). Given that Snf7 MIM1 mediates binding to both Bro1 and Doa4, we tested whether loss of Bro1 binding to Snf7 caused the almost complete loss of interaction between Doa4-VN and Snf7$^{\Delta MIM1}$-VC. Deletion of the *BRO1* gene (*bro1Δ*) appeared to reduce BiFC fluorescence derived from Doa4-VN interaction with Snf7-VC, but this reduction was not statistically significant (Fig. 1D,E), indicating that, *in vivo*, Doa4 can bind Snf7 independently of Bro1. This observation is in agreement with localization of residual Doa4 to endosomes, as seen in the absence of Bro1 (Richter et al., 2013); moreover, it is potentially enhanced – by the VC tag on the Snf7 C terminus, as C-terminal modifications are known to stabilize ESCRT-III subunits in their active conformations (Shim et al., 2007).

Overexpression of the Doa4 N-terminus causes accumulation of polymeric Snf7

We tested whether interaction between Snf7 and the Doa4 N-terminus is, indeed, the means by which we previously observed Doa4 affecting the assembly status of Snf7 *in vivo* (Johnson et al., 2017). Rate-zonal centrifugation of detergent-solubilized membranes from wild-type yeast indicated that ∼50% of membrane-associated Snf7 is polymeric, of which the bulk co-migrated through density gradients with the 440-kD protein standard ferritin (Teis et al., 2008; Fig. 2A,B). As shown previously (Johnson et al., 2017), overexpression of wild-type Doa4 increased size and abundance of Snf7 polymer assemblies (Fig. 2A,B). This effect was nullified by point mutation of the Snf7 MIM1 site that binds Doa4 (snf7$^{\Delta mim1}$; Fig. 2A,C). By contrast, in cells expressing wild-type Snf7, overexpression of Doa4$^{1\text{-}348}$ increased the size and abundance of Snf7 polymers (Fig. 2D,E), albeit not to the extent seen upon overexpression of full-length Doa4. These results are consistent with Doa4 functioning through interaction with Snf7 in order to modulate the assembly status of Snf7.

ILV membrane scission is inhibited by overexpression of the Doa4 N-terminus

We previously have shown by electron tomography and 3D modeling of yeast endosomes that Doa4 overexpression in wild-type cells inhibits ILV membrane scission (Johnson et al., 2017). The efficiency with which ESCRT-III executes membrane scission is reflected by the frequency of ILV budding profiles – invaginations that have not completed scission and are, thus, still connected to the limiting

Journal of Cell Science (2020) 133, jcs241455. doi:10.1242/jcs.241455

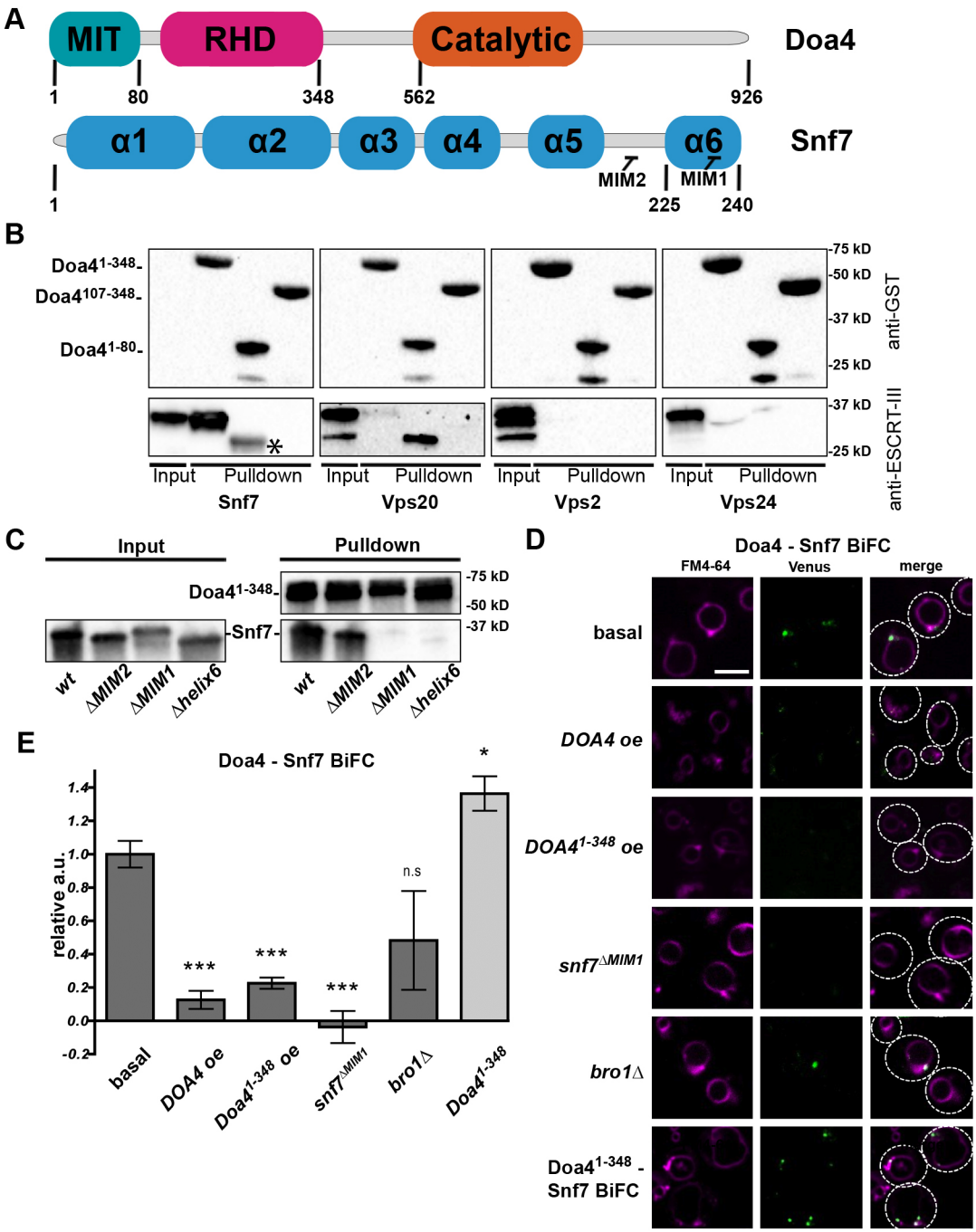

Fig. 1. Snf7 binds the N-terminus of Doa4. (A) Schematic diagram of Doa4 and Snf7. (B) Affinity isolation of GST-Doa4 fusion proteins incubated with the indicated ESCRT-III subunits. The asterisk indicates GST-Doa4$^{1\text{-}80}$, which was detected because the anti-Snf7 antiserum was raised against GST-tagged Snf7. (C) Affinity isolation of GST-Doa4$^{1\text{-}348}$ incubated with Snf7, Snf7$^{\Delta MIM2}$ (L199D, V202D), Snf7$^{\Delta MIM1}$ (L231A, L234A) or Snf7$^{\Delta\alpha6}$ (Δ226-240). (D) Live-cell BiFC fluorescence microscopy images showing the interaction of Doa4-VN or Doa4$^{1\text{-}348}$-VN (light gray bar) with Snf7-VC. Vacuolar membranes are stained with FM4-64. Dashed lines indicate cell outlines. Scale bar: 4 µm. (E) Quantification of the mean fluorescence per cell based on ≥3 independent experiments. Error bars represent the ±s.e.m.; *P≤0.05, ***P≤0.001. n.s., not significant.

endosomal membrane. Similar to our previous study (Johnson et al., 2017), we observed an average of ∼1 ILV budding profile per endosome in wild-type cells and an ∼3.5-fold increase in budding profiles upon overexpression of wild-type Doa4 (Fig. 3A,B,E; Movies 1 and 2). The robust increase in ILV budding profiles per endosome seen when Doa4 was overexpressed (wildtype+DOA4 oe) was abrogated when Doa4 was overexpressed in cells in which wild-type Snf7 was replaced with the Snf7 point-mutant that cannot bind Doa4 (*snf7*$^{\Delta MIM1}$+DOA4 oe; Fig. 3C,E; Movie 3).

The average number of budding profiles in cells expressing wild-type Snf7 was also increased by overexpression of Doa4$^{1\text{-}348}$ (Fig. 3D,E; Movie 4), though not to the degree observed upon overexpression of full-length Doa4. When plotting the frequency distribution of budding profiles per endosome we found that, in comparison to wild-type cells, more instances of multiple budding profiles occurred in response to Doa4$^{1\text{-}348}$ overexpression (Fig. 3F). Likewise, overexpression of Doa4 or Doa4$^{1\text{-}348}$ decreased the ratio of detached ILVs to ILV budding profiles; wild-type cells

Journal of Cell Science (2020) 133, jcs241455. doi:10.1242/jcs.241455

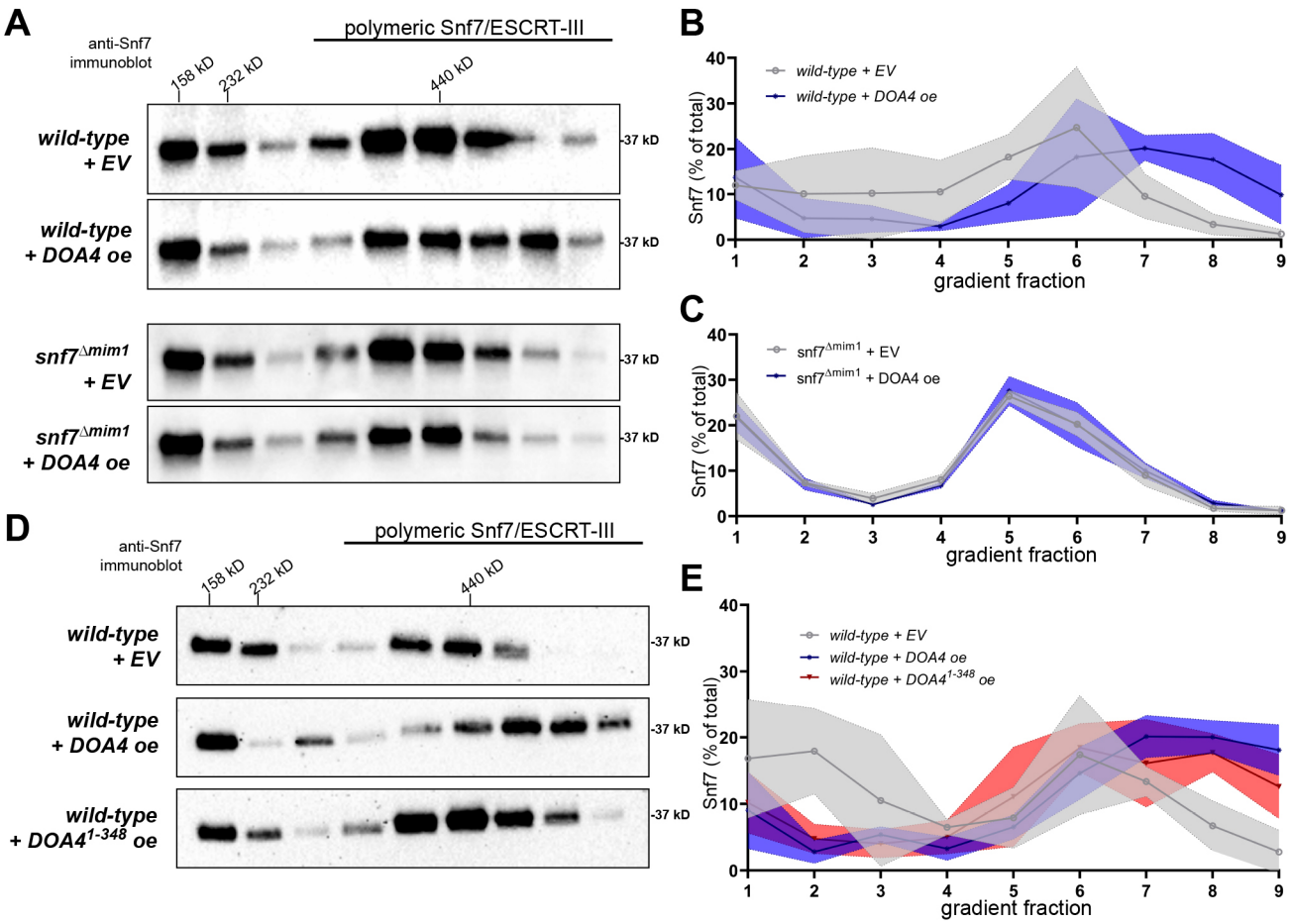

Fig. 2. Overexpression of the Doa4 N-terminus causes Snf7 polymer accumulation. (A,D) Western blots analyzing the distribution of Snf7 in fractions resolved by rate-zonal density gradient centrifugation. Indicated at the top is the migration of the protein standards aldolase (158 kDa), catalase (232 kDa) and ferritin (440 kDa). (B,C,E) Line-graphs representing the mean percentage of Snf7 in each gradient fraction examined in triplicate independent experiments. ±s.d. values of each fraction are indicated by the shaded margin surrounding each line. Statistical significance was calculated using two-tailed Student's *t*-test for each individual fraction. Differences in the levels of Snf7 protein in cells with overexpressed Doa4 (+DOA4 oe) or empty vector (+EV) were significant ($P \leq 0.05$) for fractions 7 and 8 in B, and fractions 2, 8 and 9 in E. All other differences in Snf7 protein levels were not statistically significant.

consistently exhibit a ratio of ∼30 ILVs for every budding profile observed (Fig. 3G) but, upon overexpression of full-length Doa4 or Doa4$^{1\text{-}348}$, this ratio decreased to ∼7 or ∼18 ILVs, respectively, for each budding profile observed (Fig. 3G).

We then tested whether the efficiency of ILV cargo sorting was impacted by the decreased rate of ILV membrane scission in response to overexpression of Doa4 or Doa4$^{1\text{-}348}$ by examining the model ILV cargo Cps1. In wild-type yeast expressing GFP-tagged Cps1 (GFP-Cps1), its fluorescence was observed exclusively within the vacuole lumen, which reflects sorting of Cps1 into ILVs that had been delivered into the vacuole upon fusion between endosome and vacuole (Fig. 4A). GFP-Cps1 fluorescence was also observed within the vacuole lumen in cells overexpressing either Doa4 or Doa4$^{1\text{-}348}$; however, under these conditions, fluorescence was noticeable at the vacuole membrane, which is indicative of defective sorting of Cps1 into ILVs (Fig. 4A). To quantify this mis-sorting phenotype, we utilized the luciferase reporter of intraluminal deposition (LUCID), which monitors cytosolic levels of firefly luciferase enzyme fused to Cps1 (FLuc-Cps1; Nickerson and Merz, 2015). This assay confirmed that, in wild-type cells, a small but significant amount of FLuc-Cps1 mislocalized to the vacuole membrane upon overexpression of Doa4 or Doa4$^{1\text{-}348}$ (Fig. 4B). Thus, the apparent reduction in the rate of ILV budding caused by overexpression of Doa4 or Doa4$^{1\text{-}348}$ also reduces the efficiency with which the Cps1 cargo protein is sorted into ILVs.

Doa4 inhibits Snf7 polymer association with Vps2:24 *in vitro*

The effect Doa4 overexpression *in vivo* has towards the accumulation of Snf7 polymers and inhibition of ILV membrane scission motivated us to further explore the mechanistic basis of these observations by using an *in vitro* approach. The proclivity of purified Snf7 to polymerize spontaneously on membrane-coated glass coverslips has enabled the development of quantitative assays that measure the extent to which different proteins govern assembly and turnover of polymers comprising fluorescence-labeled Snf7 (Chiaruttini et al., 2015; Mierzwa et al., 2017). We used this system to assay the extent to which Snf7 polymer dynamics are affected by the N-terminus of Doa4. For these experiments, we purified GST-Doa4$^{1\text{-}348}$ and then re-purified the Doa4$^{1\text{-}348}$ protein after eliminating GST by enzymatic cleavage.

We first tested the effect Doa4$^{1\text{-}348}$ has towards the kinetics of Snf7 polymer assembly. Previous work has shown that polymerization of fluorescence-labeled Snf7 on membrane-covered coverslips results in large patches of densely packed

Journal of Cell Science (2020) 133, jcs241455. doi:10.1242/jcs.241455

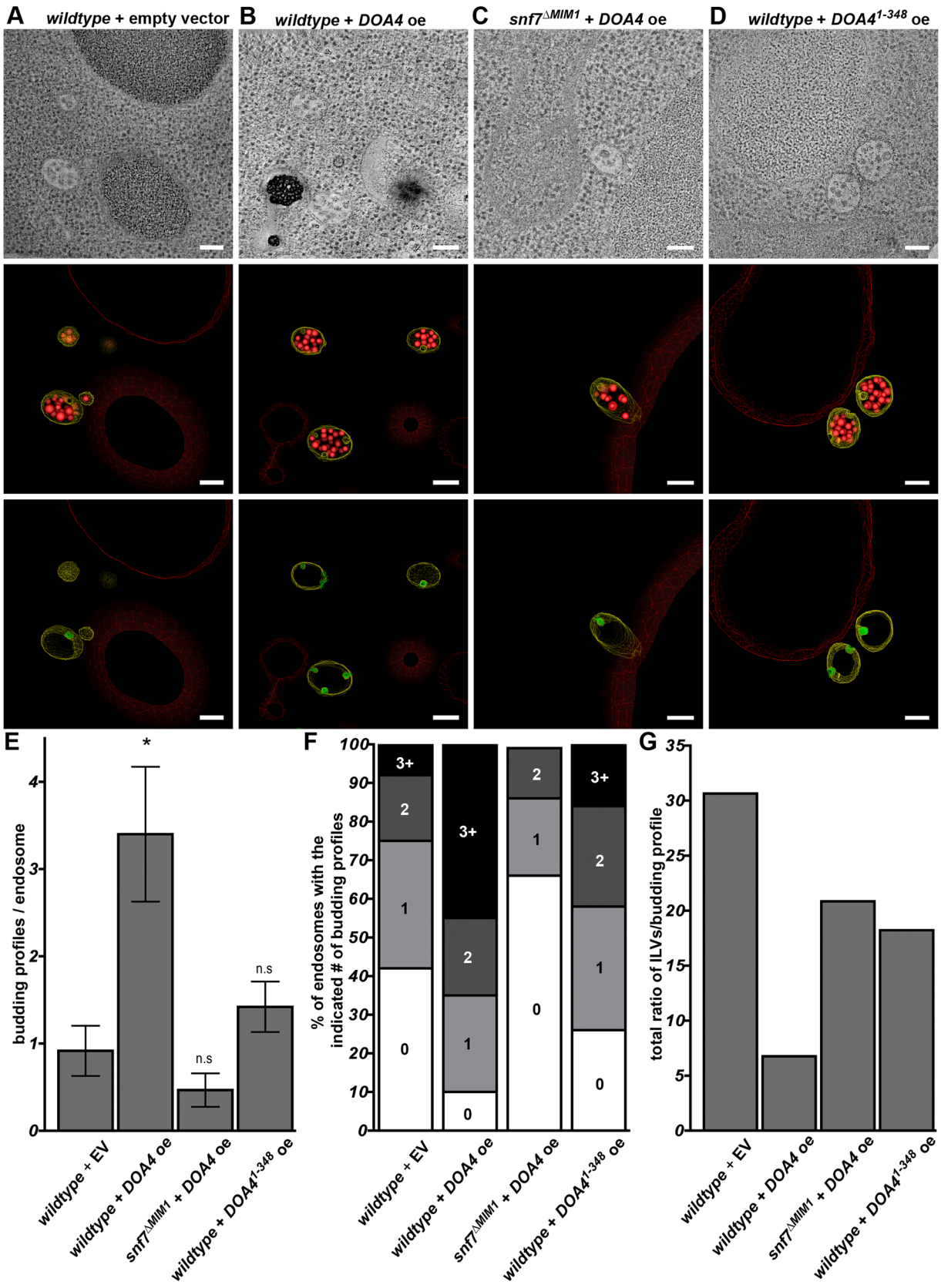

Fig. 3. See next page for legend.

spiral Snf7 filaments (Chiaruttini et al., 2015; Mierzwa et al., 2017). Fig. 5A and C show that Snf7 polymerization, reflected by the growth of these patches, was unaffected by the continuous presence of Doa4$^{1\text{-}348}$, matching our prior observations that Snf7 polymerization *in vivo* is not stimulated by Doa4 overexpression (Johnson et al., 2017).

Journal of Cell Science (2020) 133, jcs241455. doi:10.1242/jcs.241455

Fig. 3. ILV membrane scission is inhibited by overexpression of the Doa4 N-terminus. (A-D) Cross-sectional tomographic slices and 3D models obtained using electron tomography of a 250-nm thick section of a yeast cell (strain as indicated). In each model, endosome-limiting membranes are traced in yellow, detached ILVs are traced in red and ILV budding profiles are traced in green. Scale bars: 100 nm. (E) Quantification of ILV budding profiles per endosome using the tomographic models of the indicated strains. The number of endosomes analyzed under each condition are as follows: wild-type+empty vector (+EV), *n*=12; wild-type+overexpressed *DOA4* (+DOA4 oe), *n*=20; *snf7*$^{\Delta MIM1}$+*DOA4*, *n*=15; wild-type+*DOA4*$^{1-348}$, *n*=19. Error bars represent ±s.d., *$P \leq 0.05$. (F) Distribution of the percentage of endosomes observed with the indicated number of ILV budding profiles. (G) Sum of ratios of ILVs:budding profiles for all endosomes under each condition. A lower ratio of ILVs:budding profiles indicates a delay at the membrane scission step of ILV biogenesis. n.s., not significant.

Snf7 polymers on membrane-coated coverslips are stable in the presence of Vps4 and ATP alone; in the presence of Vps2:24, the combination of Vps4+ATP can catalyze disassembly of polymeric Snf7 (Mierzwa et al., 2017). To monitor the extent to which Doa4$^{1-348}$ affects Snf7 polymer disassembly kinetics, we incubated the membrane surface with fluorescence-labeled Snf7 until patches formed, then added Vps2 and Vps24 to terminate Snf7 polymer growth. We subsequently washed away soluble Snf7, Vps2 and Vps24 before adding ATP and Vps4. Doa4$^{1-348}$ was either absent throughout this experiment or present from the onset of Snf7 polymer assembly. Fig. 5B and D show that Doa4$^{1-348}$ had no effect on the rate at which Vps4 disassembled Snf7 polymers under these conditions, demonstrating that neither the catalytic inhibition of Vps4 nor steric hindrance of Vps4 access to Snf7 are responsible for Snf7 polymer accumulation in response to Doa4 overexpression in yeast (Johnson et al., 2017; Fig. 2).

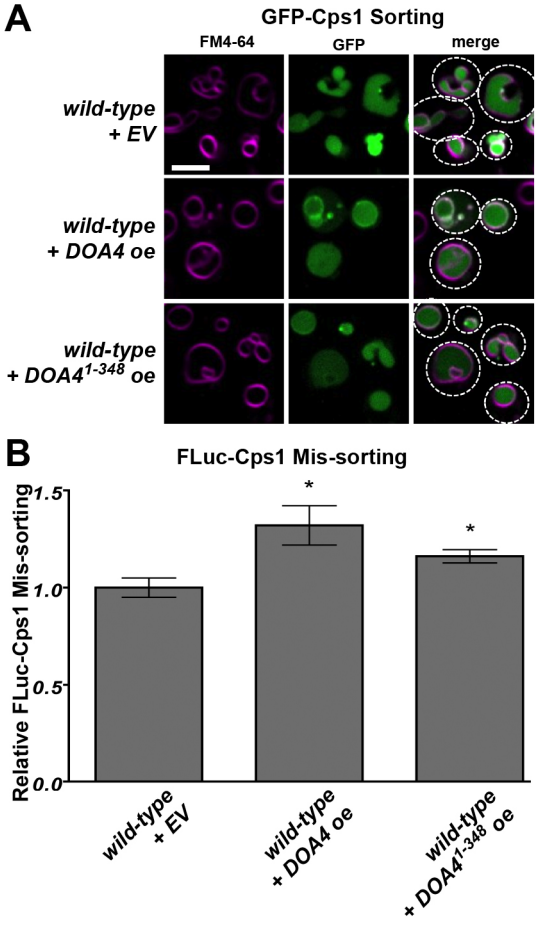

Fig. 4. ILV protein sorting is inhibited by overexpression of the Doa4 N-terminus. (A) Live-cell fluorescence microscopy of GFP-Cps1 localization (green). Vacuolar membranes are stained with FM4-64 (purple). Cell outlines are traced by dashed lines. Error bar: 4 µM. (B) FLuc-Cps1 mis-sorting was quantified using the LUCID system. Higher FLuc-Cps1 levels represent increased mis-sorting of ILV cargo. Error bars represent ±s.e.m. calculated from 4 independent experiments (*$P \leq 0.05$).

We next tested the extent to which Doa4$^{1-348}$ affects the rate at which Snf7 polymers associate with the Vps2:24 subcomplex by assembling Snf7 on the membrane surface, followed by washing away soluble Snf7 before adding Vps24 and fluorescence-labeled Vps2. Membrane association of Vps2 had been shown to depend upon Vps24 and Snf7 in this system, and the growth of Snf7 patches had been shown to be strongly suppressed upon Vps2:24 addition (Mierzwa et al., 2017), consistent with studies originally suggesting that the Vps2:24 subcomplex terminates Snf7 polymerization (Saksena et al., 2009; Teis et al., 2008). Fig. 5E and G show that the rate at which Vps2 associated with Snf7 patches was decreased when Doa4$^{1-348}$ was present continuously. Doa4$^{1-348}$ also accelerated the dissociation and/or depolymerization of Vps2 as soon as Vps4+ATP was added (Fig. 5F,H). This latter result might be a secondary effect of the lower affinity Vps2:24 has for Snf7 when Doa4$^{1-348}$ is present (Fig. 5E,G); alternatively, it might signify that Vps2:24 copolymers are preferentially targeted by Vps4 – as seen for other ESCRT-III-associated factors (Pfitzner et al., 2019 preprint). Further analysis revealed that the rate of Vps2 association with Snf7 patches was also inhibited when Doa4$^{1-348}$ is present only during Snf7 polymer assembly but washed away before addition of Vps2:24 (Fig. 5I,K). By contrast, Vps2 association kinetics were normal when Doa4$^{1-348}$ was added concomitantly with Vps2:24 (Fig. 5J,L). Therefore, the decreased association kinetics of Vps2 with Snf7 polymers seems to occur in response to Doa4 acting on Snf7, rather than the Vps2:24 subcomplex.

Overexpression of Doa4 inhibits Snf7 association with Vps2:24 and Vps4 *in vivo*

We developed an *in vivo* assay to test whether Doa4 also interferes with the native association of Snf7 and Vps2:24 at endosomal membranes in yeast. Initially, we examined cells coexpressing Vps2-VN and Snf7-VC, and found that – owing to their interaction – BiFC fluorescence localized to endosomal puncta at steady state but remained unchanged in response to Doa4 overexpression (Fig. 6A,B). This result was not surprising, given that Doa4$^{1-348}$ slowed down the rate of Vps2:24 association with Snf7 *in vitro* but did not completely block it (Fig. 5). We, therefore, assayed the kinetics of *de novo* interactions between Vps2-VN and Snf7-VC that were seen after mating yeast cells expressing either of these fusion proteins. As depicted in Fig. 6C, MATα haploid cells expressing Vps2-VN were mated with MATa haploid cells expressing Snf7-VC. Diploid zygotes exhibiting BiFC fluorescence at endosomal puncta (Fig. 6D) were observed 120 min after mating, with steadily increasing fluorescence intensity that leveled off after 300 min (Fig. 6E).

When *DOA4* was overexpressed in each haploid strain, BiFC fluorescence derived from interaction between Vps2-VN and Snf7-VC was significantly reduced after mating at 180 min and 240 min (Fig. 6E). However, at 300 min after mating, overexpression of *DOA4* had lost its effect on levels of BiFC fluorescence. Snf7$^{\Delta MIM1}$-VC, the point-mutant carrying the Doa4-binding MIM1 site point mutation in Snf7-VC, suppressed the effect of Doa4 overexpression (Fig. 6F), which is consistent with Doa4 binding to Snf7 to inhibit association with Vps2:24 at endosomal membranes.

Journal of Cell Science (2020) 133, jcs241455. doi:10.1242/jcs.241455

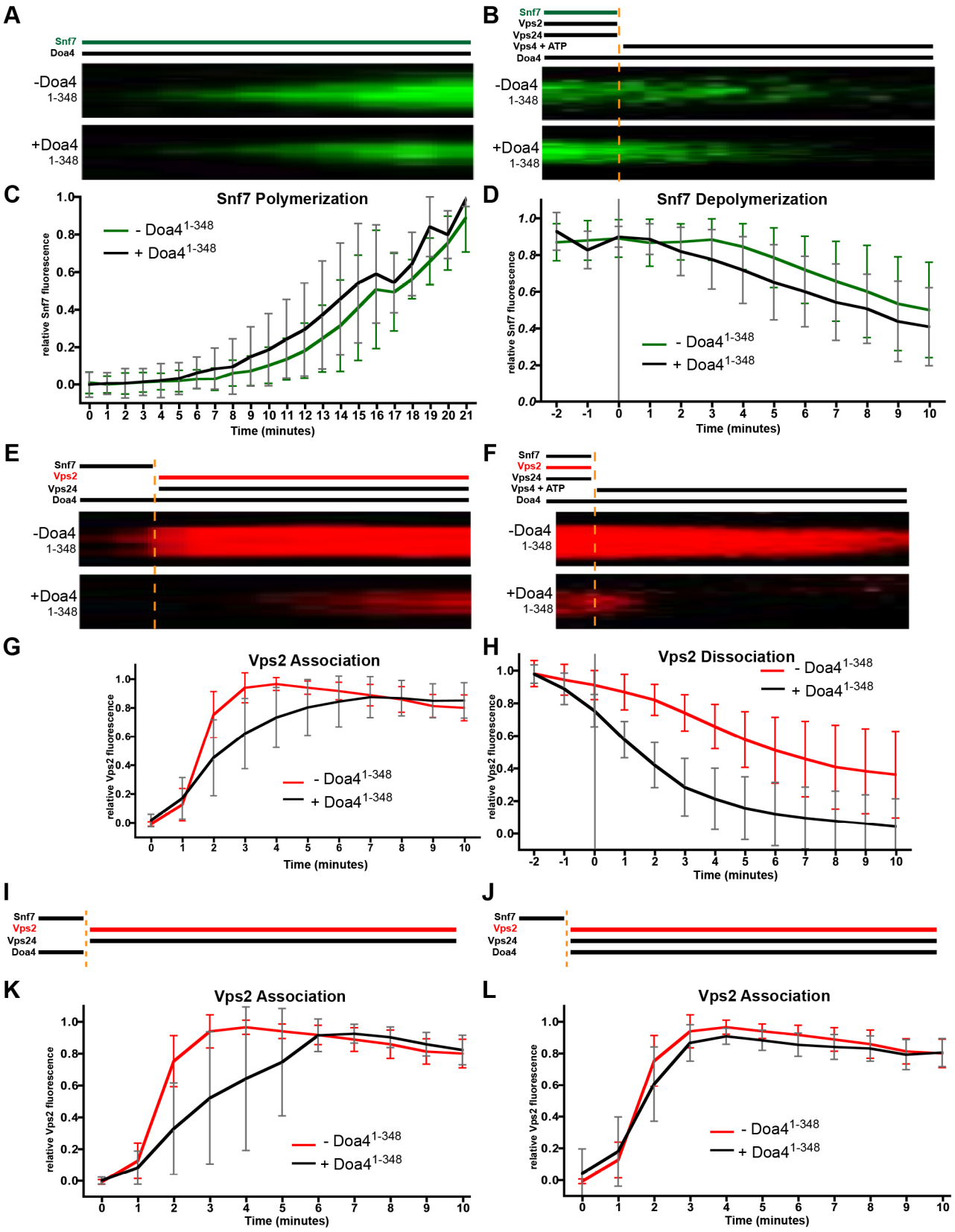

Fig. 5. See next page for legend.

The duration of 300 min that was required for Vps2-VN and Snf7-VC to achieve a steady-state level of interaction in the zygotic BiFC assay is significantly longer than the ∼10 min required for purified Vps2 and Snf7 proteins to reach a binding equilibrium *in vitro* (Fig. 5). This difference reflects the fundamental contrast between the two techniques. The binding and fluorophore

Journal of Cell Science (2020) 133, jcs241455. doi:10.1242/jcs.241455

Fig. 5. Doa4 inhibits Snf7 polymer association with Vps2:24 *in vitro*. (A) Experimental setup and kymographs from time-lapse fluorescence microscopy of representative Snf7-AlexaFluor-488 patches grown on supported lipid membranes with (+) or without (–) Doa4$^{1-348}$. (B) Kymographs of representative Snf7 patch disassembly. Snf7-AlexaFluor-488 was polymerized together with Vps2 and Vps24. At *t*=0, these were washed out, followed by the addition of ATP and Vps4. (C,D) Quantification of mean Snf7 fluorescence during polymerization (C) and depolymerization (D) of Snf7 in the presence (+) or absence (–) of Doa4$^{1-348}$, of at least 58 patches and 3 independent experiments from A and B, respectively. (E) Kymographs of Vps2 associating with representative Snf7 patches polymerized on supported lipid membranes. At *t*=0, Snf7 was washed out and Vps2-Atto-565 along with Vps24 was added. (F) Kymographs of Vps2 dissociation from representative Snf7 patches polymerized with Vps2-Atto-565 and Vps24 on supported lipid membranes. At *t*=0, these were washed out, followed by the addition of ATP and Vps4. (G,H) Quantification of mean Vps2 fluorescence during association (G) and dissociation of Vps2 (F) in the presence (+) or absence (–) of Doa4$^{1-348}$, of at least 56 patches and 3 independent experiments each from E and F, respectively. (I,J) Experimental setup for Vps2 associating with representative ESCRT-III patches. Snf7 was polymerized on supported lipid membranes. At *t*=0, Vps2-Atto-565 together with Vps24 was added. Doa4$^{1-348}$ was added either at *t*=0 (I) or during the initial Snf7 polymerization and washed out at *t*=0 (J). (K,L) Quantification of mean Vps2 fluorescence during Vps2 association in the presence (+) or absence (–) of Doa4$^{1-348}$ of at least 91 patches and 4 independent experiments each, from set-up described for I (K) and set-up described for J (L). Error bars in all graphs represent ±s.d.

maturation kinetics of Venus when the VN fragment assembles with the VC fragment (Köker et al., 2018) are several orders of magnitude slower than the kinetics with which purified ESCRT-III subunits polymerize and depolymerize (Chiaruttini et al., 2015). Thus, unlike the *in vitro* assays shown in Fig. 5, the zygotic BiFC assay does not have the temporal resolution to assess *in vivo* Vps2 association with Snf7 during a single round of ESCRT-III polymerization. Most likely, we are observing BiFC puncta at endosomes that accumulate after multiple cycles of ESCRT-III polymerization; moreover, the decreased rate of BiFC accumulation seen upon Doa4 overexpression is likely to reflect either fewer events of ESCRT-III polymerization or decreased interaction between Vps2 and Snf7 at each event.

The Vps2:24 subcomplex not only terminates Snf7 polymerization, it also recruits the Vps4 ATPase (Mierzwa et al., 2017; Teis et al., 2008). We, therefore, used our zygotic BiFC assay to test whether Doa4 overexpression inhibits the association of Vps4 with Snf7 at endosomes. BiFC fluorescence was observed starting 120 min after mating haploids that expressed Snf7-VN and Vps4-VC (Fig. 6G). Overexpression of Doa4 reduced this initial BiFC fluorescence and slowed down the rate of fluorescence accumulation, such that it did not reach steady-state levels until 360 min after mating (Fig. 6G). As was the case for interaction between Vps2-VN and Snf7-VC, mutant Snf7$^{\Delta MIM1}$-VN, carrying a point mutation of the MIM1 site, suppressed the inhibitory effect of Doa4 overexpression on this interaction (Fig. 6H). This result falls in line with our finding that Doa4 inhibits association of Snf7 with Vps2:24 because association of Vps4 with ESCRT-III depends on Vps2:24 (Babst et al., 2002; Mierzwa et al., 2017; Teis et al., 2010).

DISCUSSION

Mechanisms that regulate ESCRT-III activity are central to ensure the spatial and temporal accuracy with which this complex executes membrane scission at different intracellular sites and in different physiological processes. We have previously described a non-catalytic role for the ubiquitin hydrolase Doa4 in the regulation of ILV membrane scission by ESCRT-III at endosomes, but the mechanism behind this regulation was unknown (Johnson et al., 2017). We now present evidence that Doa4 regulates ESCRT-III activity through its direct binding to the Snf7 subunit of the complex. Our data suggest a mechanism, whereby Doa4 inhibits Snf7 association with Vps2 and Vps24 – two ESCRT-III subunits involved in polymer remodeling. Together, Vps2:24 recruit and activate the Vps4 ATPase that catalyzes ESCRT-III remodeling, which is coupled to the membrane scission mechanism (Adell et al., 2014; Cashikar et al., 2014; Sachse et al., 2004; Wemmer et al., 2011). Thus, our results might explain why Doa4 overexpression negatively regulates budding of ILVs.

The N-terminal 348-amino acid region of Doa4 that binds MIM1 within Snf7 helix α6 contains an MIT-like domain (amino acids 1-80) and RHD (amino acids 107-348). Several other proteins have MIT domains that bind MIM sites in each of the ESCRT-III subunits (Obita et al., 2007; Stuchell-Brereton et al., 2007). The MIT-like domain of Doa4 was identified on the basis of a predicted secondary structure organization similar to that of the three α helices observed in structures of MIT domains within Vps4 and Vta1 (Obita et al., 2007; Xiao et al., 2008), and because direct binding of the MIT-like region of Doa4 to the Vps20 subunit of ESCRT-III requires the MIM1 site within Vps20 helix α6 (Richter et al., 2013). However, we found that the Doa4 MIT alone is unable to bind Snf7. Likewise, Snf7 failed to bind a fragment of Doa4 that encompasses only the RHD. One explanation for these observations is that residues in both the MIT and the RHD of Doa4 directly bind Snf7 to facilitate their interaction. Alternatively, the RHD might be required to stabilize the structure of the MIT, such that it can bind to Snf7 MIM1.

The ancestral RHD function is to catalyze the conversion of cyanide to thiocyanate. However, RHDs of Doa4 and its most closely related yeast homologue Ubp5 have no catalytic activity (Cipollone et al., 2007); neither does the RHD that follows the predicted MIT in USP8, the human ortholog of Doa4. Unlike the MIT of Doa4, the MIT domain of USP8 is sufficient to bind multiple different ESCRT-III subunits, including all three isoforms of the human Snf7 ortholog CHMP4 (Row et al., 2007). This difference between the MITs of USP8 and Doa4 further indicates the possibility that the RHD provides structural support for the MIT domain within Doa4.

Unlike the MIM1 consensus sequence in Snf7 helix α6, which is required for binding of Doa4 (Fig. 1), the Vps2:24 subcomplex – via the Vps24 subunit – associates with Snf7 through electrostatic interactions involving acidic amino acids distributed along the length of Snf7 helix α4 (Banjade et al., 2019). Therefore, the ability of Doa4 to inhibit association betweenVps2:24 and Snf7 (Figs 5 and 6) does not result from direct competition between Doa4 and Vps2:24 for binding the same location in Snf7. Doa4 binding to Snf7 helix α6 might sterically hinder Vps2:24 interaction with Snf7 helix α4 or cause an allosteric conformational change in Snf7 that renders helix α4 inaccessible to Vps2:24. Defining the mechanism of Vps2:24 inhibition will depend on structural studies of ESCRT-III polymers associated with Doa4.

Like Doa4, Bro1 binds the MIM1 site within Snf7 and, as in the case of Doa4 overexpression, Bro1 overexpression inhibits Snf7 remodeling in yeast (Wemmer et al., 2011). Interestingly, Bro1 has been shown to nucleate polymerization of purified Snf7 on formvar grids (Tang et al., 2016). In contrast, we show that Doa4 has no effect on the rate at which Snf7 spontaneously polymerizes on membrane-coated coverslips. Future work using this *in vitro* system should reveal the extent to which Bro1 augments or interferes with Doa4-mediated regulation of how the Snf7 polymer associates with its remodeling factors.

Journal of Cell Science (2020) 133, jcs241455. doi:10.1242/jcs.241455

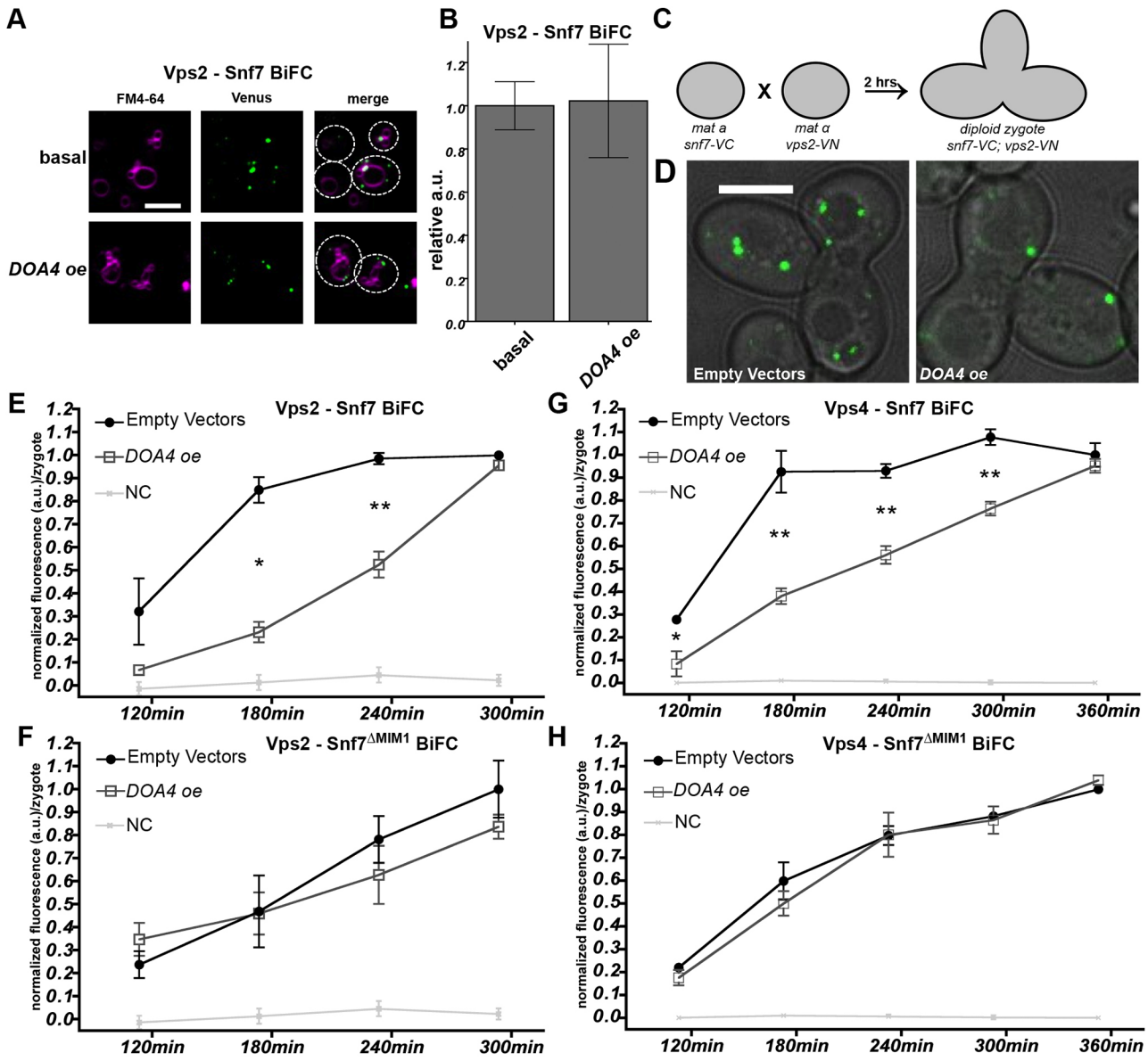

Fig. 6. Overexpression of Doa4 inhibits association of Snf7 with Vps2:24 and Vps4 *in vivo*. (A) Live-cell BiFC fluorescence microscopy showing interaction between Snf7-VC and Vps2-VN (Vps2 – Snf7 BiFC) at basal levels and in response to Doa4 overexpression (DOA4 oe). Vacuolar membranes are stained with FM4-64 (purple). Cell outlines are traced with dashed lines. Scale bar: 4 µM. (B) Quantification of mean BiFC fluorescence per cell from 4 independent experiments during an experimental set-up described in A. Error bars represent ±s.e.m.; a.u., arbitrary unit. (C) Schematic of the experimental setup for BiFC mating experiments. (D) Representative images of BiFC fluorescence derived from interaction of Vps2-VN with Snf7-VC in zygotes at 240 min after mixing haploid strains. Venus fluorescence is shown merged with the corresponding bright-field image. Scale bar: 4 µM. (E-H) Line graphs of BiFC fluorescence intensity per zygote showing interaction between Snf7-VC and Vps2-VN (E), and between Snf7-VC and Vps4-VN (Vps4–Snf7 BiFC) (F) after mixing haploid strains expressing the VN or VC fusions at *t*=0. The same analysis was performed in strains expressing the Snf7$^{\Delta MIM1}$-VC mutant (F-H). Data were normalized to BiFC fluorescence intensity at the final time-point under 'empty vector' condition. As a negative control (NC), BiFC was measured in cells expressing Snf7-VC and His2-VN, the latter of which being a cytosolic protein not involved in ESCRT-III function. Data are from at least 3 independent experiments and error bars represent ±s.e.m. (*P≤0.05, **P≤0.01).

Compared with overexpression of wild-type Doa4, overexpression of Doa4$^{1\text{-}348}$ had an intermediate inhibitory effect towards ILV membrane scission (Figs 3 and 4) and Snf7 assembly status (Fig. 2), which mirrors the intermediate inhibitory effects on both parameters in cells overexpressing catalytically inactive Doa4^{C571S} (Johnson et al., 2017). This correlation suggests a role for the Doa4 ubiquitin hydrolase activity in the regulation of ESCRT-III, although the target of this activity is unclear. Doa4 might regulate the ubiquitylation status of ESCRT-III subunits themselves, a possibility suggested in light of the finding that the ESCRT-III related protein in humans, CHMP1B, is a substrate of USP8 (Crespo-Yàñez et al., 2018). High-throughput analysis has indicated that the yeast CHMP1B ortholog Did2 is ubiquitylated in its C-terminal region, as are subunits Vps20, Vps24 and Snf7 of ESCRT-III (Swaney et al., 2013), and the C-terminus of each ESCRT-III protein mediates auto inhibition (Bajorek et al., 2009; Shim et al., 2007), raising the possibility that ubiquitylation and/or deubiquitylation of this region is a post-translational regulatory mechanism that fine-tunes the kinetics of ESCRT-III activity.

Our data show that overexpression of Doa4 in yeast inhibits association of Snf7 with the remodeling factors that are thought to drive membrane scission by ESCRT-III. However, it will be necessary to identify and mutate the Snf7-binding site in Doa4 to exclude the possibility that overabundance of Doa4 *in vivo* blocks access of Snf7 to Vps2:24 or other unknown factors in a way that does not otherwise happen when Doa4 is expressed at physiologically normal levels. The mechanism by which scission is inhibited by Doa4 can be considered in respect to the roles Vps2:24 and Vps4 have in this process. *In vitro* studies have shown that Vps2:24 remodels Snf7 polymers from flat spirals to 3D helices, a process that has been proposed to facilitate membrane constriction and/or scission by ESCRT-III (Chiaruttini et al., 2015; Henne et al., 2012). Vps2:24 association has also been proposed to enable sliding between laterally interacting Snf7 polymers, which might allow ESCRT-III to adopt different curvatures needed for its function (Banjade et al., 2019). The role of Vps4 in catalyzing Vps2:24 dissociation accelerates the growth of Snf7 polymer assemblies (Mierzwa et al., 2017) and Vps4 ATPase activity is centrally important for membrane scission by ESCRT-III (Sachse et al., 2004; Wemmer et al., 2011; Adell et al., 2014; Cashikar et al., 2014). Thus, by blocking Snf7 association with Vps2:24, which consequently blocks engagement of Snf7 with Vps4, Doa4 has the potential to stall the membrane scission mechanism of ESCRT-III. This regulatory structural role of Doa4 might serve to delay ILV budding while Doa4 functions catalytically to deubiquitylate ILV cargos, a step essential to replenish the supply of unconjugated ubiquitin that is needed to maintain cellular homeostasis (Swaminathan et al., 1999).

The regulatory role we propose for Doa4 is reminiscent of ESCRT-III regulation in humans during cytokinesis. Cytokinetic cell abscission by ESCRT-III is obstructed by CHMP4C, a CHMP4B paralog that cannot participate in the membrane scission mechanism. CHMP4C is activated through phosphorylation by the chromosomal passenger complex, in order to delay ESCRT-III-mediated cell abscission during the process of chromosomal segregation (Capalbo et al., 2012; Carlton et al., 2012). We propose that Doa4 functions in an analogous way to preserve cellular ubiquitin homeostasis by delaying ILV budding until cargo deubiquitylation is complete.

MATERIALS AND METHODS

Yeast strains and plasmid construction

Standard techniques were used for the growth and genetic manipulation of *S. cerevisiae* strains and for the construction of plasmids (Table S1). Yeast strains created for this study were constructed by one-step PCR-based integration using cassettes described in Longtine et al. (1998) and Webster et al. (2014). To construct plasmids containing GST-Doa4 fusions, PCR products containing either Doa4$^{1\text{-}348}$ or Doa4$^{107\text{-}348}$ from SEY6210 were inserted into BamHI/Xho1-digested pGEX-6P-1 or pGST parallel resulting in pCRQ0002 and pGST-DOA4^{RH}, respectively. pDCB90 was created by inserting a Doa4$^{1\text{-}348}$ PCR product including 500 bp of the *DOA4* promoter into BamHI/NotI-digested pRS202. *E. coli* expression vectors for Snf7$^{\Delta MIM2}$ (pGO613) and Snf7$^{\Delta helix6}$ (pGO557) were generated through site-directed mutagenesis of pGO547 (Wemmer et al., 2011). To create an *E. coli* expression plasmid for Vps24, a PCR product containing a Shine-Dalgarno sequence and the *VPS24* sequence from SEY6210 was ligated into EcoRI/HindIII-digested pST39 (Tan, 2001).

Pulldown of recombinant proteins from bacteria

For pulldown of Snf7 with GST-DOA4 fusion proteins, 10 ml liquid cultures of *E. coli* strain C41 (DE3) cells transformed with recombinant plasmids were induced with 0.5 mM IPTG at 20°C for 16 h. Liquid cultures were centrifuged at 1800 ***g*** for 10 min to harvest the bacterial cells, then lysed in PBS containing 1 mg/ml lysozyme (Roche), 0.25 U of Benzonase nuclease (Sigma-Aldrich) and 1 mM PMSF (Sigma-Aldrich). Lysates were sonicated at 15 W for 15 s. Triton X-100 (0.2%) was added and lysates were rotated at 4°C for 15 min before clarifying by centrifugation at 16,000 ***g*** for 10 min at 4°C. The resulting supernatant was incubated by inversion with glutathione sepharose beads (GE Healthcare) for 2 h at 4°C, then centrifuged at 5000 ***g*** for 2 min and the supernatant was discarded to eliminate unbound GST proteins. The beads were then resuspended in *E. coli* lysate containing recombinant, untagged Snf7 and rotated at 4°C for another 2 h. After four washes with PBS +0.2% TX-100, the beads were dried and boiled in Laemmli buffer. Protein samples were resolved by SDS-PAGE, transferred to a nitrocellulose membrane and western blotting was performed using anti-GST monoclonal antibodies (ThermoFisher, catalog #A-5800, 1:10,000) or rabbit polyclonal antisera raised against Snf7 (Babst et al., 1998, 1:10,000), Vps20 (Johnson et al., 2017, 1:1000), Vps24 (Babst et al., 1998), or Vps2 (1:1000). Detection of these proteins was performed using HRP-conjugated goat-anti-mouse or goat-anti-rabbit secondary antibodies (Sigma-Aldrich, catalog #A4416 or A8919, 1:3000), followed by analysis with the ChemiDoc MP imaging system (Bio-Rad).

Fluorescence microscopy and quantification

Liquid cultures of yeast strains were grown at 30°C to logarithmic phase before staining endosomal membranes with 1.6 µM FM4-64 (Invitrogen) for 25 min followed by a 90 min chase in stain-free YPD (Odorizzi et al., 2003; Vida and Emr, 1995). Live yeast cells were then observed at room temperature with an inverted fluorescence microscope (Ti2 2E PSF; Nikon) equipped with a Yokogawa CSU-X1 spinning disk confocal system and a 100× numerical aperture 1.45 oil objective (Plan Apo λ; Nikon). Images taken using an Andor iXON Ultra 512×512 EMCCD camera were acquired with Micromanager version 2.0 software and analyzed with ImageJ software (NIH). Quantification of BiFC images was performed by combining the mean and standard deviation of the fluorescence intensity per cell in at least 50 individual cells per condition. Each condition was repeated on separate days for at least three experimental replicates and the standard error of the mean was calculated. Statistical significance was calculated in GraphPad Prism software using non-paired Student's *t*-test.

Rate-zonal density gradient analysis of ESCRT-III

Gradient analysis of Snf7 polymer size and abundance was performed as described in Johnson et al. (2017). Briefly, 20-30 OD_{600} units of yeast cells were converted to spheroplasts and osmotically lysed in ice-cold PBS lysis buffer containing 0.5% Tween-20. The cells were then homogenized on ice and the membrane fraction was pelleted by centrifugation at 16,000 ***g*** at 4°C. The membrane fraction was resuspended in lysis buffer and passed through a 25-guage needle five times before loading on top of a linearized glycerol gradient (10-40%) prepared in PBS and 0.5% Tween-20. The gradient was centrifuged at 100,000 ***g*** for 4 h at 4°C. 1 ml fractions were collected and 10% trichloroacetic acid was added to precipitate the proteins on ice. Precipitates were pelleted by centrifugation at 16,000 ***g*** and washed twice by sonication in ice-cold acetone. Pellets were dried, resuspended in 50 µl of Laemmli buffer and boiled for 5 min. 15 µl of each gradient fraction protein sample was resolved by SDS-PAGE, transferred to a nitrocellulose membrane and western blotting was performed using anti-Snf7 antiserum as described above. The amount of Snf7 was quantitated in triplicate experiments using ImageJ software and the means were plotted along with the standard deviations.

Quantitative MVB cargo sorting analysis

Quantitative analysis of Cps1 sorting by LUCID was performed using the dual luciferase assay system (Promega). Cells transformed with pDN336 were harvested at early-logarithmic phase (0.3-0.4 OD_{600}). 1.2 OD_{600} units were then lysed by vortexing for 15 min with glass beads in 200 µl of the provided lysis buffer. *Firefly* and *Renilla* luciferase were analyzed in black 96-well plates using a SpectroMax M5 microplate reader (Molecular Devices). Signal from FLuc-Cps1 was normalized to the cytosolic RLuc signal to provide an internal control for plasmid expression. Three readings were performed for each strain per day on four separate days. s.e.m. was plotted and statistical significance was calculated in GraphPad Prism software using non-paired Student's *t*-test.

Electron microscopy and tomography

Liquid cultures of yeast cells were harvested at mid-logarithmic phase, vacuum filtered on 0.45-µm millipore paper, loaded into 0.5-mm aluminum hats and high-pressure frozen with a Wohlwend HPF (Wohlwend, Switzerland). Cells were freeze-substituted in an Automated Freeze-Substitution machine (Leica Vienna, Austria) at −90°C in a preparation of 0.1% uranyl acetate and 0.25% glutaraldehyde in anhydrous acetone (Giddings, 2003). Samples were then washed in pure acetone, embedded in Lowicryl HM20 resin (Polysciences), polymerized at −60°C and warmed slowly over four days. A Leica UC6 Ultra-Microtome was used to cut 80-nm or 250-nm serial semithick sections which were placed on Rhodium-plated copper slot grids (Electron Microscopy Sciences). Thick sections were labeled with 15 nm fiducial gold (British Biocell International) on both sides and mapped on a Phillips CM10 TEM at 80-kV. Dual-axis tilt series were collected from +60° to −60° with 1° increments with a Tecnai 30 (FEI) and a Gatan US4000 4k×4k CCD camera. Tilt-series were shot at 19,000× magnification with a 0.6534 nm working pixel (2× binning) and repeated at a 90° rotation for dual-axis tomography (Mastronarde, 1997). Dual-axis tomograms of endosomes and ILVs required the IMOD package (Kremer et al., 1996) for tomogram construction and modeling (3DMOD)

MVB membrane models from dual-axis electron tomograms are manually assigned from the inner leaflet, which accounts for the majority of the budding profiles. We designate budding profiles by their negative curvatures and their tendency toward asymmetric morphology. Budding profile models are drawn from the 0° rim at the outer leaflet and only counted if they have a surface area of at least 750 nm^2, or ∼50% of the mean ILV surface area (Wemmer et al., 2011). ILVs are very spherical and are measured using sphere-fitting models from the vesicle's outer leaflet (the inner leaflet of the MVB limiting membrane) and ILV diameters are measured using these sphere models. Movies were made from IMOD images and completed using QuickTime. At least 12 endosomes per strains were analyzed for the quantifications in Fig. 3. Standard deviations were plotted and statistical significance was calculated in GraphPad Prism software using a non-paired Student's *t*-test.

In vitro ESCRT-III imaging and data analysis

Snf7 (Addgene plasmid #21492), Vps2 (Addgene plasmid #21494), Vps24 (kind gift from James Hurley lab, UC Berkeley, USA) and Vps4 (Addgene plasmid #21495) were expressed and purified as previously described (Chiaruttini et al., 2015; Mierzwa et al., 2017). Snf7 was labeled with TFP-AlexaFluor-488 (Ref No. A-30005, ThermoFisher Scientific) and Vps2 was labeled with TFP-Atto-565 (Atto-Tec AD 565-3) according to the labeling procedure given by the reagent provider. The following protein concentrations were used: Snf7 500 nM, Vps2 500 nM, Vps24 500 nM, Vps4 1 µM, ATP 2 mM and $Doa4^{1-348}$ 2 µM. In general, labeled proteins were mixed 1:1 with unlabeled proteins.

Supported membrane bilayer assays were performed as described in Chiaruttini et al. (2015). Giant unilamellar vesicles (GUVs) were prepared by electroformation: 20-30 µl of a 2 mg/ml lipid solution in chloroform (DOPC: DOPS:DOPE-Atto647N:DSPEPEG(2000) Biotin, 6:4:0.01:0.003; Avanti Polar Lipids, Atto-tec) were dried on indium-tin oxide (ITO)-coated glass slides for 1 h. A growth chamber was assembled by clamping a rubber ring between the ITO-slides, filled with 500 µl of a sucrose buffer osmotically equilibrated with the experimental buffer. ITO-Slides were then connected to an AC generator set under 1 V AC (10 Hz) for 1.5 h. GUVs were stored at 4°C for at maximum one week. GUVs diluted in buffer (in 20 mM Tris pH.6.8, 200 mM NaCl and 1 mM MgCl2) were burst on a plasma-cleaned coverslip forming the bottom of a flow chamber (coverslip and sticky-Slide VI 0.4, Ibidi) to create supported bilayers. Thereafter, the chamber was passivated with casein (1 mg/ml, Sigma-Aldrich) for 10 min and washed with buffer before experiments were conducted. Subsequent changes of protein or buffer solutions in the chamber were performed via a syringe pump connected to the flow chamber. Confocal Imaging was performed on an inverted spinning disc microscope assembled by 3i (Intelligent Imaging Innovation), consisting of a Nikon base (Eclipse C1, Nikon), a 100×1.49 NA oil immersion objective and an EVOLVE EM-CCD camera (Roper Scientific Inc.). For analysis of supported bilayer experiments, 3-µm thick *Z* stacks were maximally projected using a Fiji plugin. *xy* drift of the microscopy was corrected using the plugin Turboreg and a custom-written ImageJ macro. For quantification, integrated fluorescence intensity of single patches was measured, normalized to their maximum and a kymograph was extracted.

Cell fusion of haploids for BiFC imaging

Liquid cultures of haploid yeast strains expressing BiFC fusion proteins were grown in YNB medium supplemented with amino acids at 30°C to early logarithmic phase (0.2-0.3 OD/ml). They were then combined with a liquid culture of the opposite mating type that expressed the BiFC partner protein fusion, mixed by vortexing and pelleted. Pellets were resuspended in liquid YPD and spotted onto YPD plates (time=0) which were incubated at 30°C for timepoint analysis. To prepare slides for imaging, cells were scraped from the plate, washed in water and resuspended in liquid YNB medium before spotting onto a slide for imaging at room temperature using the equipment described above. Only cells with morphology indicative of a zygote (examples in Fig. 5B) were analyzed by measuring the fluorescence intensity per zygote. Time-points for each condition were repeated on different days for at least three experimental replicates. The s.e.m. was plotted and statistical significance was calculated in GraphPad Prism software using a non-paired Student's *t*-test.

Acknowledgements

G.O. and D.B. are very grateful to Larry Gold for generously providing support. The authors thank Albert Qiu (University of Colorado, Boulder, CO) for plasmid construction and Peter Thorsness (University of Wyoming, Laramie, WY) for advice on mating yeast cells. A.-K.P. and A.R. thank the NCCR Chemical Biology for constant support during this project.

Competing interests

The authors declare no competing or financial interests.

Author contributions

Conceptualization: D.B., G.O.; Methodology: D.B., A.-K.P., M.W.; Formal analysis: D.B., A.-K.P., M.W.; Investigation: D.B., M.W.; Resources: D.B., A.R., G.O.; Writing - original draft: D.B.; Writing - review & editing: D.B., A.-K.P., A.R., G.O.; Visualization: D.B., A.-K.P., M.W.; Supervision: A.R., G.O.; Project administration: A.R., G.O.; Funding acquisition: A.R., G.O.

Funding

This work was supported by grants from the National Institutes of Health/National Institute of General Medical Sciences to G.O. (grant number: GM111335). A.R. acknowledges funding from the Swiss National Fund for Research (grant numbers: 31003A_130520, 31003A_149975 and 31003A_173087) and the European Research Council Consolidator (grant number: 311536). Deposited in PMC for release after 12 months.

Supplementary information

Supplementary information available online at
http://jcs.biologists.org/lookup/doi/10.1242/jcs.241455.supplemental

Peer review history

The peer review history is available online at
https://jcs.biologists.org/lookup/doi/10.1242/jcs.241455.reviewer-comments.pdf

References

Adell, M. A. Y., Vogel, G. F., Pakdel, M., Müller, M., Lindner, H., Hess, M. W. and Teis, D. (2014). Coordinated binding of Vps4 to ESCRT-III drives membrane neck constriction during MVB vesicle formation. *J. Cell Biol.* **205**, 33-49. doi:10.1083/jcb.201310114

Alam, S. L., Sun, J., Payne, M., Welch, B. D., Blake, B. K., Davis, D. R., Meyer, H. H., Emr, S. D. and Sundquist, W. I. (2004). Ubiquitin interactions of NZF zinc fingers. *EMBO J.* **23**, 1411-1421. doi:10.1038/sj.emboj.7600114

Babst, M., Wendland, B., Estepa, E. J. and Emr, S. D. (1998). The Vps4p AAA ATPase regulates membrane association of a Vps protein complex required for normal endosome function. *EMBO J.* **17**, 2982-2993. doi:10.1093/emboj/17.11.2982

Babst, M., Katzmann, D. J., Estepa-Sabal, E. J., Meerloo, T. and Emr, S. D. (2002). ESCRT-III: an endosome-associated heterooligomeric protein complex required for MVB sorting. *Dev. Cell* **3**, 271-282. doi:10.1016/S1534-5807(02)00220-4

Bajorek, M., Schubert, H. L., McCullough, J., Langelier, C., Eckert, D. M., Stubblefield, W.-M. B., Uter, N. T., Myszka, D. G., Hill, C. P. and Sundquist, W. I. (2009). Structural basis for ESCRT-III protein autoinhibition. *Nat. Struct. Mol. Biol.* **16**, 754-762. doi:10.1038/nsmb.1621

Banjade, S., Tang, S., Shah, Y. H. and Emr, S. D. (2019). Electrostatic lateral interactions drive ESCRT-III heteropolymer assembly. *eLife* **8**, e46207. doi:10.7554/eLife.46207

Bilodeau, P. S., Urbanowski, J. L., Winistorfer, S. C. and Piper, R. C. (2002). The Vps27p–Hse1p complex binds ubiquitin and mediates endosomal protein sorting. *Nat. Cell Biol.* **4**, 534-539. doi:10.1038/ncb815

Bowers, K., Lottridge, J., Helliwell, S. B., Goldthwaite, L. M., Luzio, J. P. and Stevens, T. H. (2004). Protein-protein interactions of ESCRT complexes in the yeast Saccharomyces cerevisiae. *Traffic* **5**, 194-210. doi:10.1111/j.1600-0854.2004.00169.x

Capalbo, L., Montembault, E., Takeda, T., Bassi, Z. I., Glover, D. M. and D'Avino, P. P. (2012). The chromosomal passenger complex controls the function of endosomal sorting complex required for transport-III Snf7 proteins during cytokinesis. *Open Biol.* **2**, 120070. doi:10.1098/rsob.120070

Carlton, J. G., Caballe, A., Agromayor, M., Kloc, M. and Martin-Serrano, J. (2012). ESCRT-III governs the Aurora B-mediated abscission checkpoint through CHMP4C. *Science* **336**, 220-225. doi:10.1126/science.1217180

Cashikar, A. G., Shim, S., Roth, R., Maldazys, M. R., Heuser, J. E. and Hanson, P. I. (2014). Structure of cellular ESCRT-III spirals and their relationship to HIV budding. *eLife* **3**, e02184. doi:10.7554/eLife.02184

Chiaruttini, N., Redondo-Morata, L., Colom, A., Humbert, F., Lenz, M., Scheuring, S. and Roux, A. (2015). Relaxation of loaded ESCRT-III spiral springs drives membrane deformation. *Cell* **163**, 866-879. doi:10.1016/j.cell.2015.10.017

Cipollone, R., Ascenzi, P. and Visca, P. (2007). Common themes and variations in the rhodanese superfamily. *IUBMB Life* **59**, 51-59. doi:10.1080/15216540701206859

Crespo-Yàñez, X., Aguilar-Gurrieri, C., Jacomin, A.-C., Journet, A., Mortier, M., Taillebourg, E., Soleilhac, E., Weissenhorn, W. and Fauvarque, M.-O. (2018). CHMP1B is a target of USP8/UBPY regulated by ubiquitin during endocytosis. *PLoS Genet.* **14**, e1007456. doi:10.1371/journal.pgen.1007456

Giddings, T. H. (2003). Freeze-substitution protocols for improved visualization of membranes in high-pressure frozen samples. *J. Microsc.* **212**, 53-61. doi:10.1046/j.1365-2818.2003.01228.x

Hanson, P. I., Roth, R., Lin, Y. and Heuser, J. E. (2008). Plasma membrane deformation by circular arrays of ESCRT-III protein filaments. *J. Cell Biol.* **180**, 389-402. doi:10.1083/jcb.200707031

Henne, W. M., Buchkovich, N. J., Zhao, Y. and Emr, S. D. (2012). The endosomal sorting complex ESCRT-II mediates the assembly and architecture of ESCRT-III helices. *Cell* **151**, 356-371. doi:10.1016/j.cell.2012.08.039

Johnson, N., West, M. and Odorizzi, G. (2017). Regulation of yeast ESCRT-III membrane scission activity by the Doa4 ubiquitin hydrolase. *Mol. Biol. Cell* **28**, 661-672. doi:10.1091/mbc.e16-11-0761

Katzmann, D. J., Babst, M. and Emr, S. D. (2001). Ubiquitin-dependent sorting into the multivesicular body pathway requires the function of a conserved endosomal protein sorting complex, ESCRT-I. *Cell* **106**, 145-155. doi:10.1016/S0092-8674(01)00434-2

Kerppola, T. K. (2006). Design and implementation of bimolecular fluorescence complementation (BiFC) assays for the visualization of protein interactions in living cells. *Nat. Protoc.* **1**, 1278-1286. doi:10.1038/nprot.2006.201

Kieffer, C., Skalicky, J. J., Morita, E., De Domenico, I., Ward, D. M., Kaplan, J. and Sundquist, W. I. (2008). Two distinct modes of ESCRT-III recognition are required for VPS4 functions in lysosomal protein targeting and HIV-1 budding. *Dev. Cell* **15**, 62-73. doi:10.1016/j.devcel.2008.05.014

Köker, T., Fernandez, A. and Pinaud, F. (2018). Characterization of split fluorescent protein variants and quantitative analyses of their self-assembly process. *Sci. Rep.* **8**, 5344. doi:10.1038/s41598-018-23625-7

Kremer, J. R., Mastronarde, D. N. and McIntosh, J. R. (1996). Computer visualization of three-dimensional image data using IMOD. *J. Struct. Biol.* **116**, 71-76. doi:10.1006/jsbi.1996.0013

Longtine, M. S., McKenzie, A., Demarini, D. J., Shah, N. G., Wach, A., Brachat, A., Philippsen, P. and Pringle, J. R. (1998). Additional modules for versatile and economical PCR-based gene deletion and modification in Saccharomyces cerevisiae. *Yeast* **14**, 953-961. doi:10.1002/(SICI)1097-0061(199807)14:10<953::AID-YEA293>3.0.CO;2-U

Luhtala, N. and Odorizzi, G. (2004). Bro1 coordinates deubiquitination in the multivesicular body pathway by recruiting Doa4 to endosomes. *J. Cell Biol.* **166**, 717-729. doi:10.1083/jcb.200403139

Mastronarde, D. N. (1997). Dual-axis tomography: an approach with alignment methods that preserve resolution. *J. Struct. Biol.* **120**, 343-352. doi:10.1006/jsbi.1997.3919

McCullough, J., Clague, M. J. and Urbé, S. (2004). AMSH is an endosome-associated ubiquitin isopeptidase. *J. Cell Biol.* **166**, 487-492. doi:10.1083/jcb.200401141

McCullough, J., Fisher, R. D., Whitby, F. G., Sundquist, W. I. and Hill, C. P. (2008). ALIX-CHMP4 interactions in the human ESCRT pathway. *Proc. Natl. Acad. Sci. USA* **105**, 7687-7691. doi:10.1073/pnas.0801567105

Mierzwa, B. E., Chiaruttini, N., Redondo-Morata, L., von Filseck, J. M., König, J., Larios, J., Poser, I., Müller-Reichert, T., Scheuring, S., Roux, A. et al. (2017). Dynamic subunit turnover in ESCRT-III assemblies is regulated by Vps4 to mediate membrane remodelling during cytokinesis. *Nat. Cell Biol.* **19**, 787-798. doi:10.1038/ncb3559

Nickerson, D. P. and Merz, A. J. (2015). LUCID: a quantitative assay of ESCRT-mediated cargo sorting into multivesicular bodies. *Traffic* **16**, 1318-1329. doi:10.1111/tra.12331

Obita, T., Saksena, S., Ghazi-Tabatabai, S., Gill, D. J., Perisic, O., Emr, S. D. and Williams, R. L. (2007). Structural basis for selective recognition of ESCRT-III by the AAA ATPase Vps4. *Nature* **449**, 735-739. doi:10.1038/nature06171

Odorizzi, G., Katzmann, D. J., Babst, M., Audhya, A. and Emr, S. D. (2003). Bro1 is an endosome-associated protein that functions in the MVB pathway in Saccharomyces cerevisiae. *J. Cell Sci.* **116**, 1893-1903. doi:10.1242/jcs.00395

Pfitzner, A.-K., Mercier, V. and Roux, A. (2019). Vps4 triggers sequential subunit exchange in ESCRT-III polymers that drives membrane constriction and fission. *bioRxiv*, 718080. doi:10.1101/718080

Richter, C. M., West, M. and Odorizzi, G. (2013). Doa4 function in ILV budding is restricted through its interaction with the Vps20 subunit of ESCRT-III. *J. Cell Sci.* **126**, 1881-1890. doi:10.1242/jcs.122499

Row, P. E., Prior, I. A., McCullough, J., Clague, M. J. and Urbé, S. (2006). The ubiquitin isopeptidase UBPY regulates endosomal ubiquitin dynamics and is essential for receptor down-regulation. *J. Biol. Chem.* **281**, 12618-12624. doi:10.1074/jbc.M512615200

Row, P. E., Liu, H., Hayes, S., Welchman, R., Charalabous, P., Hofmann, K., Clague, M. J., Sanderson, C. M. and Urbé, S. (2007). The MIT domain of UBPY constitutes a CHMP binding and endosomal localization signal required for efficient epidermal growth factor receptor degradation. *J. Biol. Chem.* **282**, 30929-30937. doi:10.1074/jbc.M704009200

Sachse, M., Strous, G. J. and Klumperman, J. (2004). ATPase-deficient hVPS4 impairs formation of internal endosomal vesicles and stabilizes bilayered clathrin coats on endosomal vacuoles. *J. Cell Sci.* **117**, 1699-1708. doi:10.1242/jcs.00998

Saksena, S., Wahlman, J., Teis, D., Johnson, A. E. and Emr, S. D. (2009). Functional reconstitution of ESCRT-III assembly and disassembly. *Cell* **136**, 97-109. doi:10.1016/j.cell.2008.11.013

Schöneberg, J., Lee, I. H., Iwasa, J. H. and Hurley, J. H. (2016). Reverse-topology membrane scission by the ESCRT proteins. *Nat. Rev. Mol. Cell Biol.* **18**, 5-17. doi:10.1038/nrm.2016.121

Schöneberg, J., Pavlin, M. R., Yan, S., Righini, M., Lee, I. H., Carlson, L. A., Bahrami, A. H., Goldman, D. H., Ren, X., Hummer, G. et al. (2018). ATP-dependent force generation and membrane scission by ESCRT-III and Vps4. *Science* **362**, 1423-1428. doi:10.1126/science.aat1839

Shim, S., Kimpler, L. A. and Hanson, P. I. (2007). Structure/function analysis of four core ESCRT-III proteins reveals common regulatory role for extreme C-terminal domain. *Traffic* **8**, 1068-1079. doi:10.1111/j.1600-0854.2007.00584.x

Stuchell-Brereton, M. D., Skalicky, J. J., Kieffer, C., Karren, M. A., Ghaffarian, S. and Sundquist, W. I. (2007). ESCRT-III recognition by VPS4 ATPases. *Nature* **449**, 740-744. doi:10.1038/nature06172

Swaminathan, S., Amerik, A. Y. and Hochstrasser, M. (1999). The Doa4 deubiquitinating enzyme is required for ubiquitin homeostasis in yeast. *Mol. Biol. Cell* **10**, 2583-2594. doi:10.1091/mbc.10.8.2583

Swaney, D. L., Beltrao, P., Starita, L., Guo, A., Rush, J., Fields, S., Krogan, N. J. and Villén, J. (2013). Global analysis of phosphorylation and ubiquitylation cross-talk in protein degradation. *Nat. Methods* **10**, 676-682. doi:10.1038/nmeth.2519

Tan, S. (2001). A modular polycistronic expression system for overexpressing protein complexes in Escherichia coli. *Protein Expr. Purif.* **21**, 224-234. doi:10.1006/prep.2000.1363

Tang, S., Buchkovich, N. J., Henne, W. M., Banjade, S., Kim, Y. J. and Emr, S. D. (2016). ESCRT-III activation by parallel action of ESCRT-I/II and ESCRT-0/Bro1 during MVB biogenesis. *eLife* **5**, e15507. doi:10.7554/eLife.15507

Teis, D., Saksena, S. and Emr, S. D. (2008). Ordered assembly of the ESCRT-III complex on endosomes is required to sequester cargo during MVB formation. *Dev. Cell* **15**, 578-589. doi:10.1016/j.devcel.2008.08.013

Teis, D., Saksena, S., Judson, B. L. and Emr, S. D. (2010). ESCRT-II coordinates the assembly of ESCRT-III filaments for cargo sorting and multivesicular body vesicle formation. *EMBO J.* **29**, 871-883. doi:10.1038/emboj.2009.408

Vida, T. A. and Emr, S. D. (1995). A new vital stain for visualizing vacuolar membrane dynamics and endocytosis in yeast. *J. Cell Biol.* **128**, 779-792. doi:10.1083/jcb.128.5.779

Webster, B. M., Colombi, P., Jäger, J. and Lusk, C. P. (2014). Surveillance of nuclear pore complex assembly by ESCRT-III/Vps4. *Cell* **159**, 388-401. doi:10.1016/j.cell.2014.09.012

Wemmer, M., Azmi, I., West, M., Davies, B., Katzmann, D. and Odorizzi, G. (2011). Bro1 binding to Snf7 regulates ESCRT-III membrane scission activity in yeast. *J. Cell Biol.* **192**, 295-306. doi:10.1083/jcb.201007018

Wolters, N. and Amerik, A. (2015). The N-terminal domains determine cellular localization and functions of the Doa4 and Ubp5 deubiquitinating enzymes. *Biochem. Biophys. Res. Commun.* **467**, 570-576. doi:10.1016/j.bbrc.2015.09.136

Xiao, J., Xia, H., Zhou, J., Azmi, I. F., Davies, B. A., Katzmann, D. J. and Xu, Z. (2008). Structural basis of Vta1 function in the multivesicular body sorting pathway. *Dev. Cell* **14**, 37-49. doi:10.1016/j.devcel.2007.10.013

SUPPLEMENTARY INFORMATION

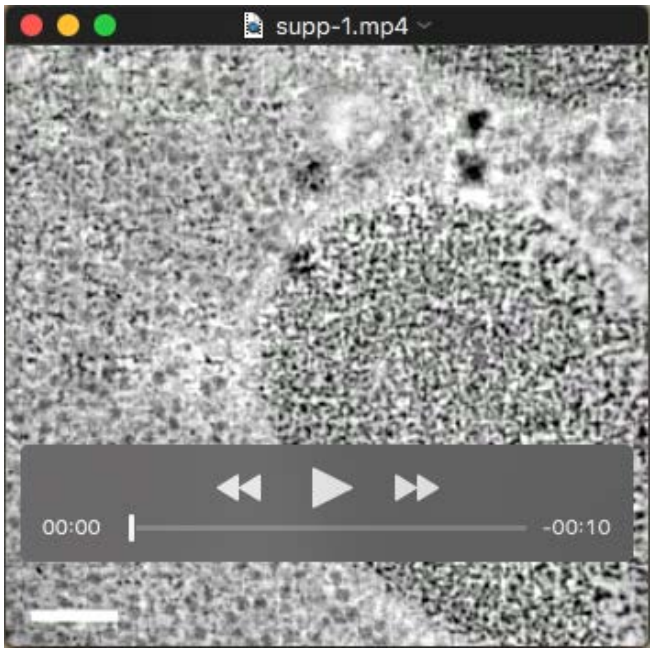

Movie 1. Representative example of the tomographic analysis of wild-type yeast transformed with an empty 2µ vector, as depicted in Fig. 3A.

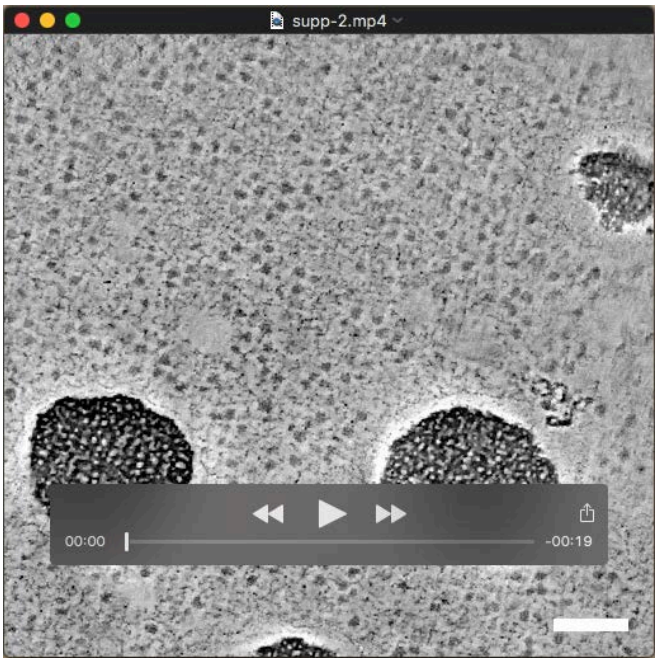

Movie 2. Representative example of the tomographic analysis of wild-type yeast transformed with 2µ *DOA4*, as depicted in Fig. 3B.

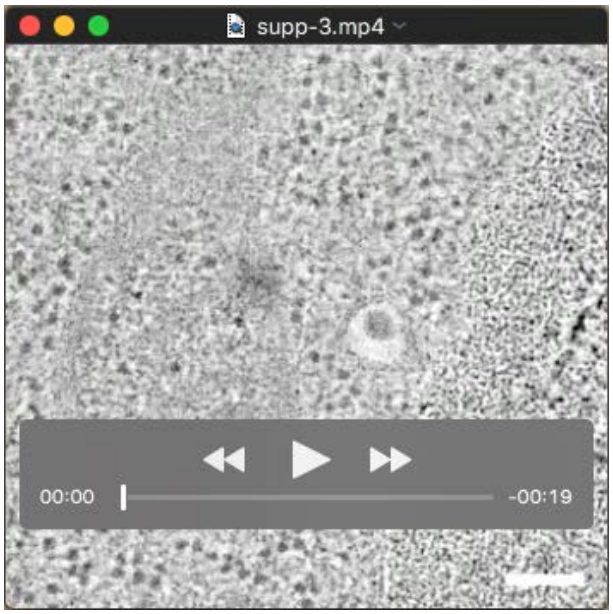

Movie 3. Representative example of the tomographic analysis of *snf7*$^{\Delta MIM1}$ yeast transformed with 2µ *DOA4*, as depicted in Fig. 3C.

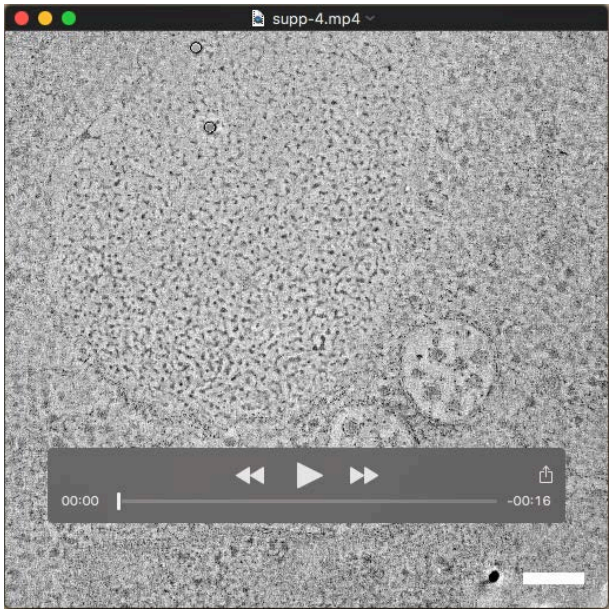

Movie 4. Representative example of the tomographic analysis of wild-type yeast transformed with 2µ *doa4*$^{1-348}$, as depicted in Fig. 3D.

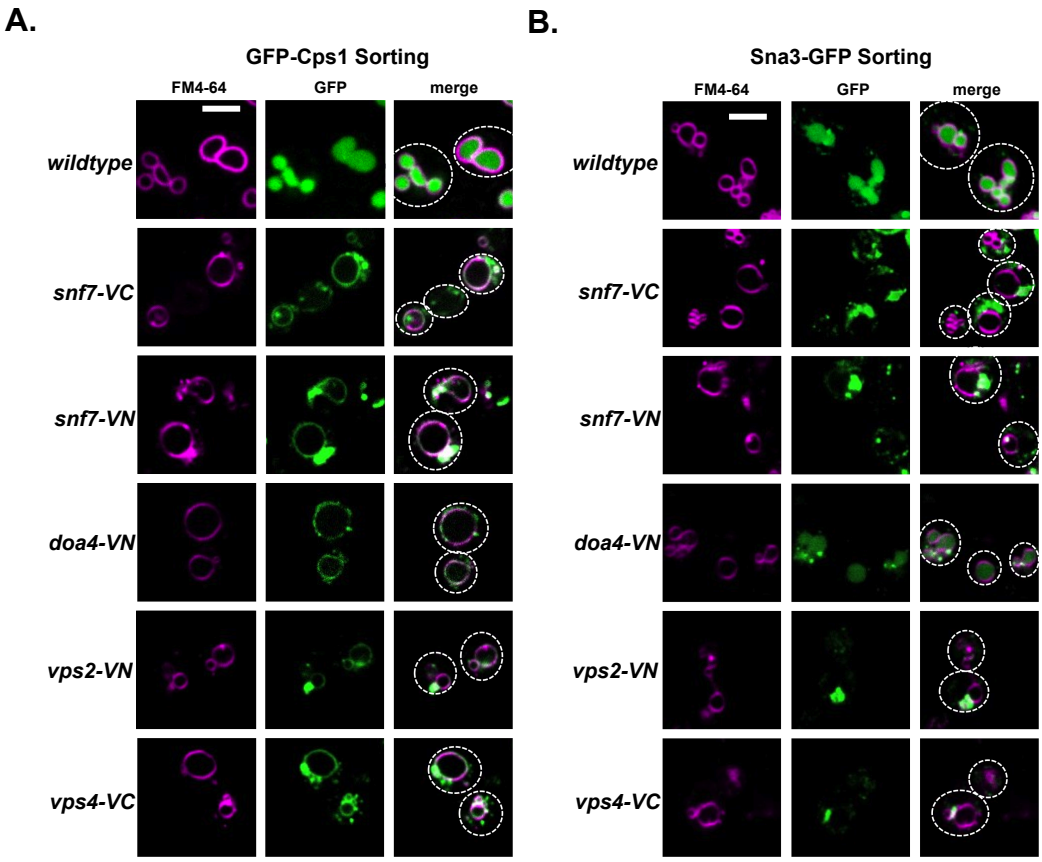

Figure S1. ILV cargo sorting in yeast expressing C-terminal VN- or VC-tagged ESCRT-III subunits

Live-cell fluorescence microscopy of GFP-Cps1 (A) or Sna3-GFP (B) localization in yeast strains expressing the indicated BiFC fusion proteins used in this study. Vacuolar and endosomal membranes are stained with FM4-64. Cell outlines are traced with the dashed lines. Bar, 4 µM.

Table S1. Yeast strains and plasmids used in this study.

Strain	Genotype	Reference
SEY6210	*MATα leu2-3,112 ura3-52 his3Δ200 trp1-Δ901 lys2-Δ801 suc2-Δ9*	Robinson et al. 1988
BWCPL1270	W303a; *snf7-VC::KANMX6*	Webster et al. 2014
BWCPL1471	W303α; *vps4-VC::KANMX6*	Webster et al. 2014
CPL1284	W303a; *snf7-VN::KANMX6*	Webster et al. 2014
GOY437	SEY6210; *doa4-VN::HIS3*	This study
GOY461	SEY6210; *snf7-VC::KANMX6 doa4-VN::HIS3*	This study
MWY25	SEY6210; *snf7$^{L231A;L234A}$::KANMX6*	Wemmer et al. 2011
DCBY100	SEY6210; *snf7-VC::KANMX6 doa4-VN::HIS3 bro1Δ::TRP1*	This study
DCBY112	SEY6210α; *vps2-VN::HIS3*	This study
DCBY116	SEY6210; *vps2-VN::HIS3 snf7-VC::KANMX6*	This study
DCBY153	SEY6210α*; his2-VN::TRP1*	This study
DCBY159	SEY6210; *snf7-VC::KanMX6 his2-VN::HIS3*	This study
DCBY163	SEY6210α; *snf7$^{L231A;L234A}$-VC::TRP1*	This study
DCBY169	SEY6210; *snf7$^{L231A;L234A}$-VC::KANMX6 doa4-VN::HIS3*	This study
DCBY175	SEY6210a; *snf7$^{L231A;L234A}$-VN::HIS3*	This study
DCBY177	SEY6210a; *snf7$^{L231A;L234A}$::KANMX6 vps2-VN::HIS3*	This study
DCBY179	SEY6210*; snf7-VC::KANMX6 doa4$^{1-348}$-VN::TRP1*	This study
DCBY180	SEY6210α; *snf7$^{L231A;L234A}$::KANMX6 vps4-VC::TRP1*	This study
DCBY181	SEY6210*; snf7 $^{L231A;L234A}$ -VC::KANMX6 doa4$^{1-348}$-VN::TRP1*	This study
DCBY183	SEY6210*; snf7-VC::KANMX6 doa4$^{1-348}$-VN::TRP1 bro1Δ::HIS3*	This study

Plasmid	Genotype	Reference
pRS202	*URA3* Ap^R *2μ*	Christianson et al. 1992
pRS426	*URA3* Ap^R *2μ*	Christianson et al. 1992
pST39	Ap^R	Tan 2001
pCR44	*URA3* Ap^R *2μ (pRS426) GFP-Doa4$^{107-348}$*	This study
pCR52	*URA3* Ap^R *2μ (pRS426) GFP-Doa4$^{1-348}$*	This study
pCR58	*URA3* Ap^R *2μ (pRS426) GFP-Doa4*	This study
pCR152	Ap^R (pST39) *GST-Doa4$^{1-80}$*	Richter et al. 2013
pCRQ2	Ap^R (pST39) *GST-Doa4$^{1-348}$*	This study
pDCB17	*LEU2* Ap^R *2μ (pRS415) GFP-Cps1*	This study
pDCB90	*URA3* Ap^R (pRS202) *Doa4$^{1-348}$*	This study
pDN336	TRP1 Ap^R (pDN614) *PGK1$_{pr}$::RLuc CPS1$_{pr}$::FLuc-CPS*	Shideler et al., 2015
pGO289	*URA3* Ap^R *(pRS202) DOA4*	Luhtala and Odorizzi 2004
pGO511	Ap^R (pST39) VPS*20*	Johnson et al. 2017
pGO515	Ap^R (pST39) *VPS24*	This study
pGO516	Ap^R (pST39) *VPS2*	Richter et al. 2013
pGO547	Ap^R (pST39) *SNF7*	Wemmer et al. 2011
pGO557	Ap^R (pST39) *Snf7$^{1-225}$*	This study
pGO560	Ap^R (pST39) *Snf7^{L231A,L234A}*	Richter et al. 2013
pGO613	Ap^R (pST39) *Snf7^{L199D,V202D}*	This study
pGO640	*URA3* Ap^R *2μ (pRS426) GFP-Doa4$^{1-80}$*	Richter et al. 2013
pGST-DOA4^{RH}	Ap^R (pST39) *GST-Doa4$^{107-348}$*	This study